NANO LETTERS

pubs.acs.org/NanoLett

Letter

High-Throughput All-Optical Determination of Nanorod Size and Orientation

Zachary J. O'Dell, Megan Knobeloch, Sara E. Skrabalak,* and Katherine A. Willets*

Cite This: *Nano Lett.* 2024, 24, 7269−7275

Read Online

ACCESS | Metrics & More | Article Recommendations | Supporting Information

ABSTRACT: As a single-particle characterization technique, optical microscopy has transformed our understanding of structure−function relationships of plasmonic nanoparticles, but the need for *ex-situ*-correlated electron microscopy to obtain structural information handicaps an otherwise exceptional high-throughput technique. Here, we present an all-optical alternative to electron microscopy to accurately and quickly extract structural information about single gold nanorods (Au NRs) using calcite-assisted localization and kinetics (CLocK) microscopy. Color CLocK images of single Au NRs allow scattering from the longitudinal and transverse plasmon modes to be imaged simultaneously, encoding spectral data in CLocK images that can then be extracted to obtain Au NR size and orientation. Moreover, through the use of convolutional neural networks, Au NR length, width, and aspect ratio can be predicted directly from color CLocK images within ∼10% of the true value measured by electron microscopy.

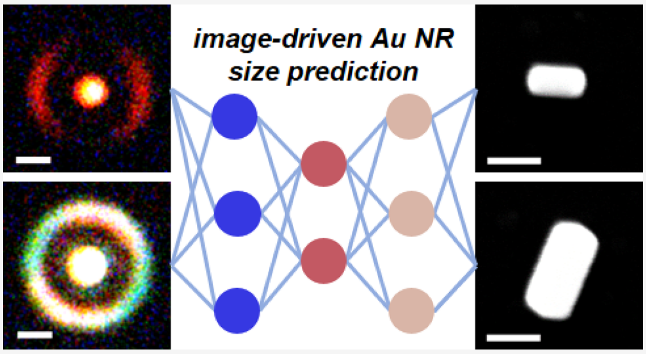

KEYWORDS: *single-particle, plasmonic nanoparticles, dark-field microscopy, polarization-resolved spectroscopy, RGB colorimetric analysis, image-based machine learning*

Single-particle characterization techniques have revolutionized our understanding of the structure−function relationships that exist at the nanoscale, allowing for better design, synthetic control, and use of nanomaterials in a wide range of applications.[1−5] Dark-field (DF) microscopy is one technique driving this progress, where tens to hundreds of single plasmonic metal nanoparticles can be simultaneously monitored due to their ability to strongly scatter light.[6−11] However, due to the diffraction-limited nature of optical microscopy, information about nanoparticle structure and morphology is lost during DF studies, which is problematic, as the optical properties of plasmonic nanoparticles are dependent on their size, shape, composition, and local environment.[12−16] To correlate the measured optical response to nanoparticle structure, *ex-situ* electron microscopy is often required, which is time-consuming, costly, and destructive and, most importantly, limits the efficiency of otherwise high-throughput DF microscopy experiments.[17−20] Thus, optical single-particle techniques must strive to identify structural differences in plasmonic nanoparticles without the need for correlated electron microscopy.

One strategy to encode structural information about nanoparticle size and shape into optical images is to use point-spread function (PSF) engineering, in which an optic is added into the emission path of a microscope and transforms diffraction-limited spots into more information-rich images. For example, Sönnichsen et al. inserted a rotating wedge polarizer into a DF microscope equipped with a color camera, creating ring patterns that were diagnostic of nanoparticle shape and size.[21] However, no correlated single-particle electron microscopy experiments were performed; therefore, the structures responsible for each pattern were inferred from ensemble electron microscopy measurements. Our group recently developed a related technique, termed calcite-assisted localization and kinetics (CLocK) microscopy, in which a rotating birefringent calcite crystal is inserted into the detection path of a DF microscope, modifying the PSF of the scattered light such that a polarization-averaged diffraction-limited spot is surrounded by a polarization-resolved intensity ring (Figures 1A, S1). Using correlated electron microscopy, we demonstrated the ability to differentiate gold nanospheres and nanorods of varying size in a heterogeneous sample.[22] More recently, Bouchal et al. used a Q-plate in the emission path of their microscope to create multilobed PSFs, from which they extracted the polarization anisotropy.[23] They used correlated electron microscopy and optical images to construct

Received: March 14, 2024
Revised: June 5, 2024
Accepted: June 5, 2024
Published: June 7, 2024

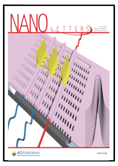

ACS Publications

https://doi.org/10.1021/acs.nanolett.4c01261
Nano Lett. 2024, 24, 7269−7275

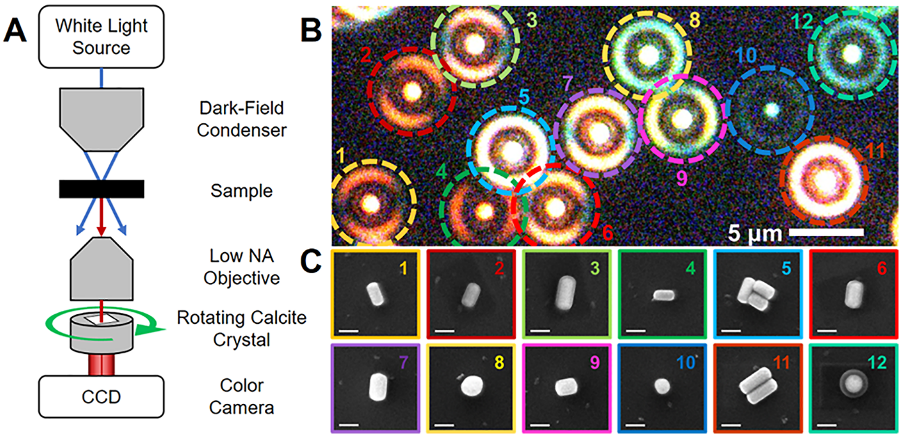

Figure 1. Shape and size heterogeneity in a mixture of Au NRs and Au NSs captured using color CLocK microscopy. (A) Schematic of the CLocK microscopy setup where a rotating birefringent calcite crystal is inserted into the infinity space of the microscope. (B) Wide-field color CLocK image of a mixture of single Au NRs, Au NSs, and aggregated Au NRs. The image contrast is set to highlight the $e_{\perp}$ ring from the dimmest particle (#10). Scale bar: 5 μm. (C) Correlated SEM image of the nanoparticles imaged in B, numerically labeled, as well as color-coded. Scale bars = 100 nm.

a calibration curve for nanorods of varying sizes, allowing them to directly calculate the aspect ratio (AR) from optical images, without the need for correlated SEM.

While PSF engineering has demonstrated the ability to differentiate shapes or extract nanorod ARs from a single image, there has not yet been a demonstration of generating full structural parameters of single nanoparticles using this approach. Instead, approaches based on spectral analysis have shown the most success in extracting structural information. For example, Landes et al. successfully predicted the length and width of gold nanorods (Au NRs) within ~10% of their true size using DF scattering spectra combined with machine learning models.[24] However, DF spectroscopy is typically a lower throughput technique, in which nanoparticles must be aligned within the slit of the spectrometer. This approach limits the number of particles that can be captured within a single acquisition (typically <3 for randomly dispersed particles), while also requiring integration times from seconds to minutes to obtain high signal-to-noise spectra. This temporal limitation is a challenge for tracking dynamic changes in multiple nanorod structures *in situ* and in real time. To combat this, red/green/blue (RGB) colorimetric analysis of DF scattering images allows for fast, dynamic processes to be observed on a large number of nanoparticles without the need for full spectral analysis.[25−31] For example, Long et al. showed that RGB colorimetric analysis of DF scattering can determine the size of Au nanospheres (NSs) within 5 nm of the size determined by electron microscopy.[32] However, diffraction-limited RGB imaging is less suited for the size determination of anisotropic structures due to the presence of multiple plasmon modes associated with different structural axes. Thus, most single-particle structure−function studies rely on electron microscopy for generating structural information about samples, limiting our ability to monitor structure *in situ* and/or in samples incompatible with electron microscopy.

Herein, we demonstrate that color CLocK microscopy can accurately predict the size and AR of single gold nanorods using only a single RGB image as input. Our ability to achieve this milestone is based upon the multidimensional spectral, scattering intensity, particle orientation, and anisotropy information encoded in a single-color CLocK image. Briefly, CLocK images are constructed by using a birefringent calcite crystal to separate the nanoparticle scattering into a spatially invariant ordinary ray ($o_{\parallel}$) and spatially displaced extraordinary ray ($e_{\perp}$) (Figure S1A). As the calcite crystal rotates, the $e_{\perp}$ ray sweeps out a ring around the diffraction-limited $o_{\parallel}$ ray. At each orientation of the calcite crystal, the polarization of both $e_{\perp}$ and $o_{\parallel}$ rotates while remaining mutually perpendicular (Figure S1B). We can individually fit the background-subtracted R, G, and B intensity (I) of the $e_{\perp}$ ring as a function of calcite crystal orientation (θ), as determined using eq 1:

$$I_{\theta} \propto 1 + M\cos\{2(\theta - \varphi)\} \tag{1}$$

where φ is the orientation of the nanoparticle and M is the modulation depth, a term that defines nanoparticle anisotropy and ranges from zero (isotropic) to one (dipole-like).[22] Specific information regarding background subtraction and data analysis can be found in the Supporting Information (Figures S2 and S3 and associated text).

Figure 1B shows a color CLocK image from a mixture of Au NSs, NRs, and NR aggregates as well as their corresponding electron micrographs (Figure 1C). To produce sufficiently high signal-to-noise from the dimmest particle in this region (particle 10), we use a camera integration time of 600 ms. While this integration time saturates the $o_{\parallel}$ (Table S1), thus limiting its utility for kinetic or super-resolution analysis,[22] structural information is encoded in the unsaturated $e_{\perp}$ ring and allows for structural differentiation, even by eye. For example, the PSFs of the spherical particles (8, 10, and 12) have uniform color rings with consistent intensity, with the color red-shifting and overall scattering intensity increasing as the particle size increases (Table S1 and associated discussion), as expected.[33,34] Smaller nanorods (particles 1, 2, and 4) show a broken ring pattern, whereas larger nanorods (particles 3, 6, 7, and 9) have multicolored ring patterns with the lower energy component oriented along the long axis, consistent with previous wavelength-dependent polarization-resolved single-particle measurements.[33,35−38] Aggregates (particles 5 and 11) appear whitish in color and have a higher scattering intensity than their single-particle counterparts (Table S1 and associated discussion). Importantly, these behaviors are expected based upon previous literature, in which a series of images are acquired at unique polarizations,[33,36,39] but the CLocK image captures these trends in a single image, allowing rapid evaluation (by eye) of nanoparticle distributions in heterogeneous mixtures.

To test the ability of CLocK to predict nanorod size, Au NRs of various dimensions were synthesized by modifying a previously reported seed-mediated method, then spin-coated onto a conductive, optically transparent indium tin oxide (ITO)-coated glass coverslip in order to carry out correlated optical and electron microscopy (Figure S4, Table S2).[40] Figure 2A,B show the correlated SEM and color CLocK image of a 142 nm × 80 nm Au NR, where the modulation of color from red-orange to green in the optical image reveals the orientation of the Au NR. Unlike the polarization-averaged $o_{\parallel}$, where scattering from the more intense longitudinal peak dominates and leads to a red-orange diffraction-limited spot, the polarization-resolved nature of the $e_{\perp}$ ring separates the intensity contributions of the longitudinal and transverse plasmon modes into a multicolor $e_{\perp}$ ring, allowing for the more intense longitudinal mode to be observed at a θ value of 87° ($e_{\perp\ \text{long}}$) and the less intense transverse plasmon mode to be observed at a θ value of 177° ($e_{\perp\ \text{trans}}$). This variation is shown in the RGB polar plot shown in Figure 2C, which individually plots the R, G, and B intensity components of the $e_{\perp}$ ring as a function of θ, where M and φ values can be calculated by using eq 1 (Table S3, particle 2). Moreover, because we know the orientation of the rod (φ), we can determine the R, G, and B intensity at any arbitrary polarization, allowing us to compare the spectral properties of the nanorod when the calcite crystal is aligned with the long or short axis of the rod. For example, at $e_{\perp\ \text{long}}$, the R intensity contribution is greater than that of the G intensity contribution (R/G ratio of 2.69), consistent with the longitudinal plasmon mode dominating at this polarization; however, as θ approaches $e_{\perp\ \text{trans}}$, the R/G ratio gradually decreases, reaching a minimum value of 0.82 at $e_{\perp\ \text{trans}}$ and showing that the transverse mode is now the dominant spectral feature.

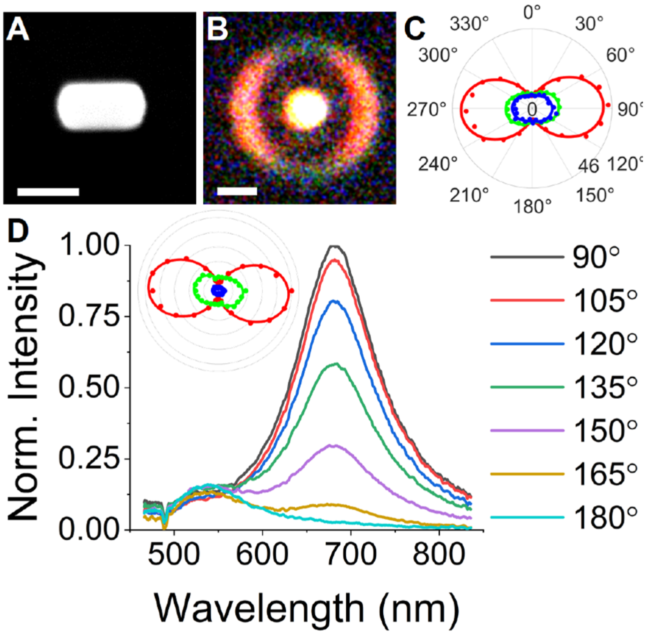

Figure 2. Correlated SEM, color CLocK, and polarization-resolved scattering data for a single Au NR. (A) SEM image of a 142 × 80 nm Au NR oriented at 87°. Scale bar = 100 nm. (B) Color CLocK image of the Au NR. Scale bar: 1 μm. (C) RGB polar plot extracted from the color CLocK image in B. (D) Polarization-resolved dark-field scattering spectra taken at various linear polarizer orientations. Inset of an RGB polar plot extracted from the polarization-resolved scattering data in D.

To validate this interpretation, Figure 2D shows a series of polarization-resolved spectra for the same nanorod. At a linear polarizer orientation of 90° ($\sim e_{\perp\ \text{long}}$), the difference in intensity between the longitudinal and transverse peak is at a maximum, but as the linear polarizer is rotated toward larger angles, this difference gradually decreases as the intensity of the longitudinal peak decreases. At a linear polarizer orientation of 180° ($\sim e_{\perp\ \text{trans}}$), the longitudinal peak is virtually absent compared to the more intense transverse peak, leading to the green color observed at $e_{\perp\ \text{trans}}$ in the CLocK image. By multiplying the polarization-resolved spectra by the quantum efficiency spectrum of the color charged-coupled device (CCD) used to capture color CLocK images (Figure S5), an RGB polar plot similar to the one in Figure 2C can be made (Figure 2D inset). The polar plots show similar modulations in R and G intensity as a function of θ that qualitatively agree with the color CLocK RGB polar plots, indicating that the color information captured in CLocK images reflects the single-particle spectral information well (Figure S6).

Figure 3 shows a cropped wide-field, background-subtracted color CLocK image of six variously sized Au NRs, as well as their correlated SEM images (Table S3). The associated single-particle spectral data are shown in Figure S7. Once again, the orientation of the red intensity component can be used to determine NR orientation, but more importantly the color differences in the $e_{\perp}$ ring reveal size differences between small (3 and 4), medium (1, 2, and 5), and large (6) Au NRs, which originate from differences in the single-particle scattering

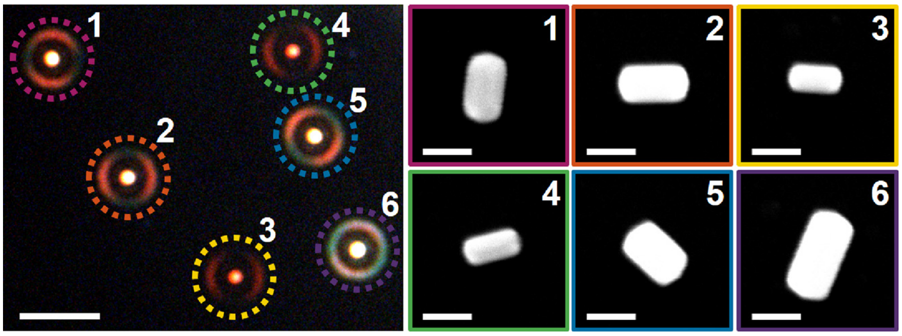

Figure 3. Correlated color CLocK–SEM images for various sized single Au NRs. Correlated images are both color-coded and numerically labeled. Color CLocK scale bar = 5 μm. SEM scale bar = 100 nm.

spectra (Figure S7). By visually comparing the color CLocK $e_{\perp}$ ring signature to the Au NR width measured using SEM, we observe that the G intensity along $e_{\perp\,\text{trans}}$ becomes more apparent as the Au NR width increases, which is expected as the transverse plasmon mode becomes more intense (Figure 3 and Table S3).[41] Similarly, increases in Au NR AR can be inferred from the R/G intensity ratio observed along $e_{\perp\,\text{long}}$, which should increase as the Au NR AR increases and the longitudinal peak red-shifts to larger wavelengths, although this trend will begin to break down due to limitations of the CCD, as discussed below.[42−45] Despite this limitation, color CLocK microscopy captures a unique and diagnostic signal from Au NRs that other forms of microscopy cannot capture (Figure S8). As such, color CLocK is a powerful high-throughput tool for nanoparticle feature screening.

Quantitatively, how the $e_{\perp}$ ring color varies as a function of Au NR dimensions is shown in Figure 4. For Au NRs of constant width and increasing length, the G intensity along $e_{\perp\,\text{trans}}$ remains more or less constant once the AR is large enough such that the longitudinal and transverse modes are sufficiently separated, minimizing bleed over between the red and green channels in the CCD (Figures 4A, S9, Table S4). As AR increases and the longitudinal mode red-shifts beyond the sensitivity of our CCD, an initial increase in the R intensity along $e_{\perp\,\text{long}}$ is observed, followed by a plateau, and eventual decrease as AR increases (Figure S10). Conversely, for Au NRs of constant length and increasing width, the G intensity along $e_{\perp\,\text{trans}}$ increases, while the R intensity along $e_{\perp\,\text{long}}$ decreases relative to the green intensity (Figures 4B, S11, Table S5). To relate $e_{\perp}$ ring parameters with the Au NR size, 735 SEM-correlated color CLocK images of Au NRs were fit using eq 1, and select parameters were plotted against the measured Au NR dimensions (Figure 4C−F). For bins containing multiple nanoparticles, both the absolute and relative standard deviations of the variables presented in Figure 4C−F can be found in Figure S12.

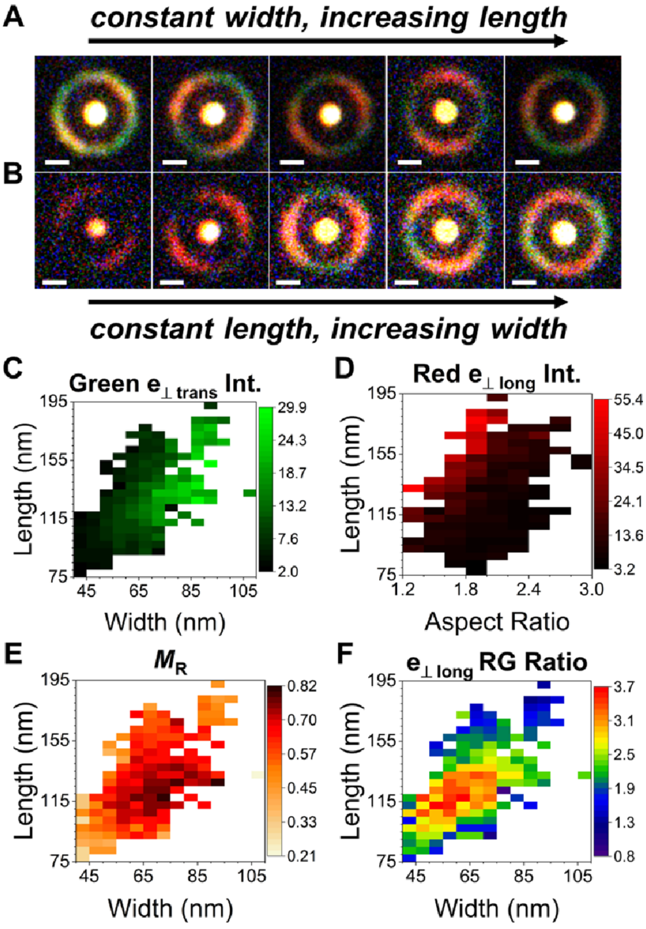

Figure 4. Trends in color CLocK images as Au NR size changes. (A) Color CLocK images of Au NRs of constant width and increasing length. (B) Color CLocK images of Au NRs of constant length and increasing width. Scale bars: 1 μm. (C−F) Various RGB parameters extracted from eq 1 plotted as a function of Au NR length, width, and/or aspect ratio. Green and red intensity values at θ orientations $e_{\perp\,\text{trans}}$ and $e_{\perp\,\text{long}}$ are plotted in C and D, respectively. Mean values are plotted for bins containing multiple nanoparticles, and white bins represent particle sizes that were not measured.

One predictable trend emerges where the G intensity along $e_{\perp\,\text{trans}}$ increases as a function of Au NR width (Figure 4C). However, for other $e_{\perp}$ ring parameters, nonlinear trends emerge as a function of Au NR dimensions, making predicting Au NR size difficult. For example, R intensity along $e_{\perp\,\text{long}}$ increases with increasing Au NR length, but shows little intensity for Au NRs with large ARs (Figure 4D). This observation can be attributed to the inability of our CCD to detect photons at wavelengths larger than 700 nm, where the longitudinal peak of Au NRs with large ARs is expected to be found (Figure S10). Thus, only a fraction of the R intensity from the longitudinal peak is detected, as seen in Au NR #6 of Figure 3, where the color along $e_{\perp\,\text{long}}$ appears pale red as a result of the longitudinal peak being centered at 770 nm (Figure S7). This limitation of the CCD similarly affects the value of the red modulation depth (M_R): while we expect M to be >0.7 for nanorods, we see lower than expected M values for rods with the higher ARs (Figure 4E). Additionally, the M_R values appear lower than expected for rods with lower ARs, as the close proximity between the longitudinal and transverse peaks leads to the transverse peak being partially detected in the red channel of the CCD (Figures 4B, S11). These limitations of the CCD lead to an optimal pocket in the R/G intensity ratio along $e_{\perp\,\text{long}}$ as a function of Au NR length and width, even though the R/G intensity along $e_{\perp\,\text{long}}$ would be expected to increase with increasing length (Figure 4F).

While we can identify size-dependent trends in the data above, predicting absolute Au NR size via the parametrization of the $e_{\perp}$ ring is challenging due to the multidimensional nature of the data set, the convolution of some parameters, degeneracy between some parameters, and the limitations of the CCD. However, even by eye, we can tell that differences in the $e_{\perp}$ ring images encode differences in Au NRs' size and even aggregation (Figure S13). Thus, we turn to machine learning methods to predict Au NR size, where convolutional neural networks (CNNs) determine structural parameters directly from the CLocK images, as shown in Figure 5 (see SI for full details).[46] These tools are uniquely suited to handle multidimensional data sets. Figure 5A shows a confusion matrix for 193 particles after training the CNN with 1093 color CLocK images of single Au NRs, Au NR aggregates, and other misshapen Au particles. Of the 157 particles that were single nanorods, 9 were misidentified (5.7%), while 148 were correctly classified (94.3%). Of the non-rod-like structures (36 particles), half were misidentified as rods. The incorrect classification of these structures most likely originates from the samples used to train the algorithm, where rods of varying sizes were the dominant species; therefore, the CNN had limited

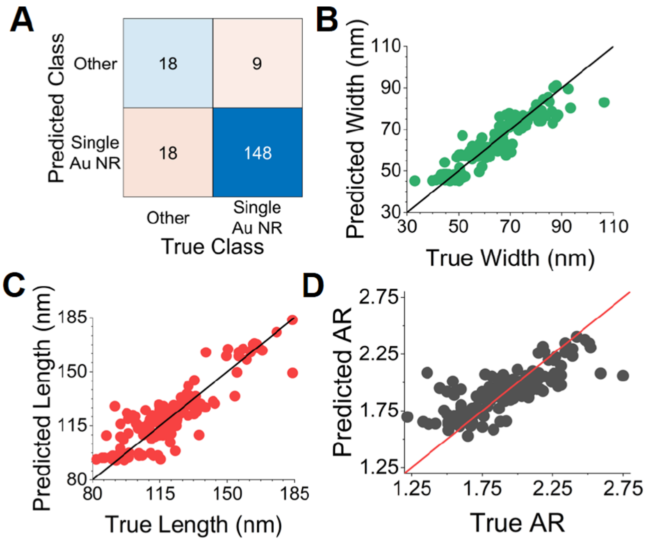

Figure 5. Imaged-based CNN models to predict the Au NR aggregation state and size. (A) Classification model to predict the Au NR aggregation state. Classification accuracy = 86%. (B) Regression model to predict the Au NR width. RMSE = 5.2 nm. RMSPE = 8.4%. (C) Regression model to predict Au NR length. RMSE = 9.9 nm. RMSPE = 8.9%. (D) Predicted aspect ratio (AR) calculated from the predicted length and width. RMSE = 0.18. RMSPE = 10.7%.

data about aggregates or misshapen structures. We expect that training the CNN using a more structurally diverse population will improve the accuracy of the assignments.

Regression CNNs were trained to predict Au NR width and length directly using 847 color CLocK images to train the model and 150 to validate the results. Initial attempts to train a CNN to directly predict the AR were unsuccessful, as shown in Figure S14. Next, we tested a CNN trained to predict the length and width simultaneously and then calculated the AR from these two values (Figure S15). While the predicted length and width values showed reasonable agreement with the experimentally determined values, the calculated AR tended to converge to a limited range of values, overestimating the AR when the true value was small and underestimating it when the true value was large (Figure S15).

Interestingly, training individual CNNs to predict either the width or the length of the Au NR independently was far more successful. The CNN width and length predictions had root mean-squared error (RMSE) values of 5.2 and 9.9 nm, respectively, which correspond to root mean-squared percent errors (RMSPE) of 8.4% and 8.9% (Figure 5B,C). These errors are lower than the errors found for the CNN trained to evaluate the length and width at the same time (Figure S15C). Calculating the AR from these values led to better agreement with the experimental values than the previously trained models (Figures S14, S15C), with an RMSE of 0.18 and an RMSPE of 10.7% (Figure 5D). We believe the performance differences between these various CNNs is most likely due to the spectral overlap and limited range of the CCD, which causes leakage between the green and red channels when the longitudinal and transverse peaks are close or suppression of the red scattering intensity when the longitudinal plasmon extends into the near-IR. This leads to potential degeneracies in CLocK images of different sized rods, which the algorithm struggles to differentiate when asked to fit certain parameters alone (e.g., AR, Figure S14) or two values at the same time (e.g., length and width, Figure S15). However, this issue is easily surmounted by training two separate models, as shown in Figure 5, and then using these values to calculate the AR. Examples of Au NRs whose length and/or width were predicted incorrectly by the two independently trained CNNs are shown in Figure S16, where factors such as low signal-to-noise, misshapen Au NRs, and the close proximity of a second Au NR may also influence the predicted dimensions (Table S6). Despite these outliers, our results indicate that we generate accurate structural data with ∼10% error for the majority of the nanorods in our sample, providing a key step forward in our ability to measure shape and size using only a single optical image.

In conclusion, we demonstrate that color CLocK microscopy is a valuable technique to differentiate between differently sized Au NRs directly within optical microscopy experiments. The short integration time and wide-field capabilities of the technique make color CLocK microscopy a viable high-throughput option for not only screening single plasmonic nanoparticles of various size and shape but also monitoring real-time changes to nanoparticle structure during dynamic processes (as shown in previous work).[22] These capabilities are especially relevant given the inherent heterogeneity found in nanoparticle samples, which now can be optically screened without requiring electron microscopy, allowing for rapid identification of the desired particle shape (Figure 1). We have also shown that color CLocK images capture differences in Au NR size (and scattering spectra), allowing for qualitative differences in Au NR size to be visually assessed, even when using an inexpensive CCD. For applications in which increased spectral accuracy is required, a series of bandpass filters can be used to acquire spectrally resolved CLocK images, which will be demonstrated in future work.

By using CNNs to analyze color CLocK images, our current model can be trained to predict Au NR length, width, and thus AR within an RMSPE of approximately 10%. We note that this is our initial attempt to demonstrate the ability of machine learning to augment optical imaging and provide structural information beyond what can be visually assessed. As we acquire more data and apply increasingly sophisticated algorithms, we foresee the ability to translate this approach to other researchers without the need for each lab to perform its own training and validation. Moreover, expanding the training set to include not only misshapen particles and aggregates but also more diverse shapes and sized particles will further help define the limits of what can be learned by combining CLocK microscopy with machine learning. Ultimately, we believe that these studies form the foundation of the next-generation of single-particle optical experiments, further increasing our understanding of structure−function relationships at the nanoscale.

■ ASSOCIATED CONTENT

Supporting Information

The Supporting Information is available free of charge at https://pubs.acs.org/doi/10.1021/acs.nanolett.4c01261.

CLocK microscopy schematics, bulk dimensional analysis of Au NR size using electron microscopy, the quantum efficiency spectrum of the CCD, additional correlated CLocK-SEM-DF scattering spectra data, additional CNN model results, common abbreviations, reagents and materials used, experimental details of Au NR synthesis, data collection, and data analysis (PDF)

AUTHOR INFORMATION

Corresponding Authors

Sara E. Skrabalak − *Department of Chemistry, Indiana University−Bloomington, Bloomington, Indiana 47405, United States;* orcid.org/0000-0002-1873-100X; Email: sskrabal@indiana.edu

Katherine A. Willets − *Department of Chemistry, Temple University, Philadelphia, Pennsylvania 19122, United States;* orcid.org/0000-0002-1417-4656; Email: kwillets@temple.edu

Authors

Zachary J. O'Dell − *Department of Chemistry, Temple University, Philadelphia, Pennsylvania 19122, United States;* orcid.org/0000-0002-7779-596X

Megan Knobeloch − *Department of Chemistry, Indiana University−Bloomington, Bloomington, Indiana 47405, United States;* orcid.org/0009-0007-8070-5789

Complete contact information is available at:
https://pubs.acs.org/10.1021/acs.nanolett.4c01261

Notes

The authors declare no competing financial interest.

ACKNOWLEDGMENTS

This material is based upon work supported by the National Science Foundation under the Centers for Chemical Innovation Grant No. CHE 2221062 for the Center for Single-Entity Nanochemistry and Nanocrystal Design (CSENND) and National Science Foundation Graduate Research Fellowship under Grant No. 2038235. The authors would like to thank the members of CSENND for their valuable insights and feedback throughout this project.

REFERENCES

(1) Wang, W.; Tao, N. Detection, Counting, and Imaging of Single Nanoparticles. *Anal. Chem.* **2014**, *86* (1), 2−14.

(2) Zijlstra, P.; Orrit, M. Single Metal Nanoparticles: Optical Detection, Spectroscopy and Applications. *Rep. Prog. Phys.* **2011**, *74* (10), No. 106401.

(3) Olson, J.; Dominguez-Medina, S.; Hoggard, A.; Wang, L.-Y.; Chang, W.-S.; Link, S. Optical Characterization of Single Plasmonic Nanoparticles. *Chem. Soc. Rev.* **2015**, *44* (1), 40−57.

(4) Sambur, J. B.; Chen, P. Approaches to Single-Nanoparticle Catalysis. *Annu. Rev. Phys. Chem.* **2014**, *65* (1), 395−422.

(5) Wahab, O. J.; Kang, M.; Unwin, P. R. Scanning Electrochemical Cell Microscopy: A Natural Technique for Single Entity Electrochemistry. *Current Opinion in Electrochemistry* **2020**, *22*, 120−128.

(6) Liu, M.; Chao, J.; Deng, S.; Wang, K.; Li, K.; Fan, C. Dark-Field Microscopy in Imaging of Plasmon Resonant Nanoparticles. *Colloids Surf., B* **2014**, *124*, 111−117.

(7) Shang, J.; Fan, J.; Qin, W.; Li, K. Single-Particle Measurements of Nanocatalysis with Dark-Field Microscopy. *Catalysts* **2022**, *12* (7), 764.

(8) Ringe, E.; Sharma, B.; Henry, A.-I.; D. Marks, L.; Duyne, R. P. V. Single Nanoparticle Plasmonics. *Phys. Chem. Chem. Phys.* **2013**, *15* (12), 4110−4129.

(9) Xie, T.; Jing, C.; Long, Y.-T. Single Plasmonic Nanoparticles as Ultrasensitive Sensors. *Analyst* **2017**, *142* (3), 409−420.

(10) Sundaresan, V.; Monaghan, J. W.; Willets, K. A. Monitoring Simultaneous Electrochemical Reactions with Single-particle Imaging. *ChemElectroChem.* **2018**, *5* (20), 3052−3058.

(11) Sundaresan, V.; Monaghan, J. W.; Willets, K. A. Visualizing the Effect of Partial Oxide Formation on Single Silver Nanoparticle Electrodissolution. *J. Phys. Chem. C* **2018**, *122* (5), 3138−3145.

(12) Lu, X.; Rycenga, M.; Skrabalak, S. E.; Wiley, B.; Xia, Y. Chemical Synthesis of Novel Plasmonic Nanoparticles. *Annu. Rev. Phys. Chem.* **2009**, *60* (1), 167−192.

(13) Willets, K. A.; Van Duyne, R. P. Localized Surface Plasmon Resonance Spectroscopy and Sensing. *Annu. Rev. Phys. Chem.* **2007**, *58* (1), 267−297.

(14) Wang, L.; Hasanzadeh Kafshgari, M.; Meunier, M. Optical Properties and Applications of Plasmonic-Metal Nanoparticles. *Adv. Funct. Mater.* **2020**, *30* (51), No. 2005400.

(15) Boken, J.; Khurana, P.; Thatai, S.; Kumar, D.; Prasad, S. Plasmonic Nanoparticles and Their Analytical Applications: A Review. *Appl. Spectrosc. Rev.* **2017**, *52* (9), 774−820.

(16) L. Nehl, C.; H. Hafner, J. Shape-Dependent Plasmon Resonances of Gold Nanoparticles. *J. Mater. Chem.* **2008**, *18* (21), 2415−2419.

(17) Slaughter, L.; Chang, W.-S.; Link, S. Characterizing Plasmons in Nanoparticles and Their Assemblies with Single-particle Spectroscopy. *J. Phys. Chem. Lett.* **2011**, *2* (16), 2015−2023.

(18) Novo, C.; Funston, A. M.; Pastoriza-Santos, I.; Liz-Marzán, L. M.; Mulvaney, P. Spectroscopy and High-Resolution Microscopy of Single Nanocrystals by a Focused Ion Beam Registration Method. *Angew. Chem., Int. Ed.* **2007**, *46* (19), 3517−3520.

(19) McMahon, J. M.; Wang, Y.; Sherry, L. J.; Van Duyne, R. P.; Marks, L. D.; Gray, S. K.; Schatz, G. C. Correlating the Structure, Optical Spectra, and Electrodynamics of Single Silver Nanocubes. *J. Phys. Chem. C* **2009**, *113* (7), 2731−2735.

(20) Henry, A.-I.; Bingham, J. M.; Ringe, E.; Marks, L. D.; Schatz, G. C.; Van Duyne, R. P. Correlated Structure and Optical Property Studies of Plasmonic Nanoparticles. *J. Phys. Chem. C* **2011**, *115* (19), 9291−9305.

(21) Schubert, O.; Becker, J.; Carbone, L.; Khalavka, Y.; Provalska, T.; Zins, I.; Sönnichsen, C. Mapping the Polarization Pattern of Plasmon Modes Reveals Nanoparticle Symmetry. *Nano Lett.* **2008**, *8* (8), 2345−2350.

(22) Monaghan, J. W.; O'Dell, Z. J.; Sridhar, S.; Paranzino, B.; Sundaresan, V.; Willets, K. A. Calcite-Assisted Localization and Kinetics (CLocK) Microscopy. *J. Phys. Chem. Lett.* **2022**, *13* (45), 10527−10533.

(23) Bouchal, P.; Dvořák, P.; Hrtoň, M.; Rovenská, K.; Chmelík, R.; Šikola, T.; Bouchal, Z. Single-Shot Aspect Ratio and Orientation Imaging of Nanoparticles. *ACS Photonics* **2023**, *10* (9), 3331−3341.

(24) Shiratori, K.; Bishop, L. D. C.; Ostovar, B.; Baiyasi, R.; Cai, Y.-Y.; Rossky, P. J.; Landes, C. F.; Link, S. Machine-Learned Decision Trees for Predicting Gold Nanorod Sizes from Spectra. *J. Phys. Chem. C* **2021**, *125* (35), 19353−19361.

(25) Zhi Zhang, H.; Sheng Li, R.; Fei Gao, P.; Wang, N.; Lei, G.; Zhi Huang, C.; Wang, J. Real-Time Dark-Field Light Scattering Imaging to Monitor the Coupling Reaction with Gold Nanorods as an Optical Probe. *Nanoscale* **2017**, *9* (10), 3568−3575.

(26) Sun, S.; Gao, M.; Lei, G.; Zou, H.; Ma, J.; Huang, C. Visually Monitoring the Etching Process of Gold Nanoparticles by KI/I2 at Single-Nanoparticle Level Using Scattered-Light Dark-Field Microscopic Imaging. *Nano Res.* **2016**, *9* (4), 1125−1134.

(27) Yano, Y.; Nisougi, M.; Yano-Ozawa, Y.; Ohguni, T.; Ogawa, A.; Maeda, M.; Asahi, T.; Zako, T. Detection of Gold Nanoparticles Aggregation Using Light Scattering for Molecular Sensing. *ANAL. SCI.* **2019**, *35* (6), 685−690.

(28) Xiao, L.; Wei, L.; He, Y.; Yeung, E. S. Single Molecule Biosensing Using Color Coded Plasmon Resonant Metal Nanoparticles. *Anal. Chem.* **2010**, *82* (14), 6308−6314.

(29) Zhou, J.; Gao, P. F.; Zhang, H. Z.; Lei, G.; Zheng, L. L.; Liu, H.; Huang, C. Z. Color Resolution Improvement of the Dark-Field Microscopy Imaging of Single Light Scattering Plasmonic Nanoprobes for microRNA Visual Detection. *Nanoscale* **2017**, *9* (13), 4593−4600.

(30) Hao, J.; Xiong, B.; Cheng, X.; He, Y.; Yeung, E. S. High-Throughput Sulfide Sensing with Colorimetric Analysis of Single Au–Ag Core–Shell Nanoparticles. *Anal. Chem.* **2014**, *86* (10), 4663–4667.

(31) Gu, Z.; Jing, C.; Ying, Y.-L.; He, P.; Long, Y.-T. In Situ High Throughput Scattering Light Analysis of Single Plasmonic Nanoparticles in Living Cells. *Theranostics* **2015**, *5* (2), 188–195.

(32) Jing, C.; Gu, Z.; Ying, Y.-L.; Li, D.-W.; Zhang, L.; Long, Y.-T. Chrominance to Dimension: A Real-Time Method for Measuring the Size of Single Gold Nanoparticles. *Anal. Chem.* **2012**, *84* (10), 4284–4291.

(33) Islam, M. M.; Hossen, M. M.; Koschny, T.; Hillier, A. C. Shape- and Orientation-Dependent Scattering of Isolated Gold Nanostructures Using Polarized Dark-Field Microscopy. *J. Phys. Chem. C* **2021**, *125* (21), 11478–11488.

(34) Jain, P. K.; Lee, K. S.; El-Sayed, I. H.; El-Sayed, M. A. Calculated Absorption and Scattering Properties of Gold Nanoparticles of Different Size, Shape, and Composition: Applications in Biological Imaging and Biomedicine. *J. Phys. Chem. B* **2006**, *110* (14), 7238–7248.

(35) Cao, X.; Lei, G.; Feng, J.; Pan, Q.; Wen, X.; He, Y. A Novel Color Modulation Analysis Strategy through Tunable Multiband Laser for Nanoparticle Identification and Evaluation. *Anal. Chem.* **2018**, *90* (4), 2501–2507.

(36) Liu, J. J.; Yan, H. H.; Zhang, Q.; Gao, P. F.; Li, C. M.; Liang, G. L.; Huang, C. Z.; Wang, J. High-Resolution Vertical Polarization Excited Dark-Field Microscopic Imaging of Anisotropic Gold Nanorods for the Sensitive Detection and Spatial Imaging of Intracellular microRNA-21. *Anal. Chem.* **2020**, *92* (19), 13118–13125.

(37) Huang, Y.; Ferhan, A. R.; Kim, D.-H. Tunable Scattered Colors over a Wide Spectrum from a Single Nanoparticle. *Nanoscale* **2013**, *5* (17), 7772–7775.

(38) Chaudhari, K.; Pradeep, T. Spatiotemporal Mapping of Three Dimensional Rotational Dynamics of Single Ultrasmall Gold Nanorods. *Sci. Rep* **2014**, *4* (1), 5948.

(39) Biswas, S.; Nepal, D.; Park, K.; Vaia, R. A. Orientation Sensing with Color Using Plasmonic Gold Nanorods and Assemblies. *J. Phys. Chem. Lett.* **2012**, *3* (18), 2568–2574.

(40) Ye, X.; Zheng, C.; Chen, J.; Gao, Y.; Murray, C. B. Using Binary Surfactant Mixtures To Simultaneously Improve the Dimensional Tunability and Monodispersity in the Seeded Growth of Gold Nanorods. *Nano Lett.* **2013**, *13* (2), 765–771.

(41) Huang, Y.; Kim, D.-H. Dark-Field Microscopy Studies of Polarization-Dependent Plasmonic Resonance of Single Gold Nanorods: Rainbow Nanoparticles. *Nanoscale* **2011**, *3* (8), 3228–3232.

(42) Woo Moon, S.; Vuka Tsalu, P.; Won Ha, J. Single-particle Study: Size and Chemical Effects on Plasmon Damping at the Interface between Adsorbate and Anisotropic Gold Nanorods. *Phys. Chem. Chem. Phys.* **2018**, *20* (34), 22197–22202.

(43) Liu, J. J.; Wen, S.; Yan, H. H.; Cheng, R.; Zhu, F.; Gao, P. F.; Zou, H. Y.; Huang, C. Z.; Wang, J. The Accurate Imaging of Collective Gold Nanorods with a Polarization-Dependent Dark-Field Light Scattering Microscope. *Anal. Chem.* **2022**, *95* (2), 1169–1175.

(44) Schmucker, A. L.; Harris, N.; Banholzer, M. J.; Blaber, M. G.; Osberg, K. D.; Schatz, G. C.; Mirkin, C. A. Correlating Nanorod Structure with Experimentally Measured and Theoretically Predicted Surface Plasmon Resonance. *ACS Nano* **2010**, *4* (9), 5453–5463.

(45) Qiu, Y.; Liu, Y.; Wang, L.; Xu, L.; Bai, R.; Ji, Y.; Wu, X.; Zhao, Y.; Li, Y.; Chen, C. Surface Chemistry and Aspect Ratio Mediated Cellular Uptake of Au Nanorods. *Biomaterials* **2010**, *31* (30), 7606–7619.

(46) Masson, J.-F.; Biggins, J. S.; Ringe, E. Machine Learning for Nanoplasmonics. *Nat. Nanotechnol.* **2023**, *18* (2), 111–123.